IEEE Access
Multidisciplinary ⋮ Rapid Review ⋮ Open Access Journal

Received 29 April 2023, accepted 20 May 2023, date of publication 23 May 2023, date of current version 7 June 2023.

Digital Object Identifier 10.1109/ACCESS.2023.3279275

RESEARCH ARTICLE

Intelligent Computed Torque Control With Recurrent Legendre Fuzzy Neural Network for Permanent-Magnet Assisted Synchronous Reluctance Motor

FAA-JENG LIN[1], (Fellow, IEEE), MING-SHI HUANG[2], CHUNG-YU HUNG[1], AND YU-CHEN CHIEN[1]

[1]Department of Electrical Engineering, National Central University, Taoyuan City 32001, Taiwan
[2]Department of Electrical Engineering, National Taipei University of Technology, Taipei City 10608, Taiwan

Corresponding author: Faa-Jeng Lin (linfj@ee.ncu.edu.tw)

This work was supported by the National Science and Technology Council of Taiwan under Grant MOST 110-2221-E-008-054-MY3.

ABSTRACT The goal of this research is to develop an intelligent controlled permanent-magnet assisted synchronous reluctance motor (PMASynRM) drive system by utilizing an intelligent computed torque control with recurrent Legendre fuzzy neural network (ICTCRLFNN), in order to adjust the nonlinear and time-varying control specifications of the motor. The team first proposes an ANSYS Maxwell-2D dynamic model that contains a maximum torque per ampere (MTPA) control PMASynRM drive. A lookup table (LUT) is composed of the finite element analysis (FEA) results, which bring about the current angle of command within the MTPA. Subsequently, the team designs a computed torque control (CTC) system to control the speed reference command. Creating a working CTC for practical applications is quite complex because the detailed system dynamics, which includes the unpredictability of the PMASynRM drive system, is not available beforehand. Thus, this study suggests that a recurrent Legendre fuzzy neural network (RLFNN) can act as a close substitute for the CTC to resolve its existing complications. Furthermore, the team modifies an adaptive compensator to proactively adjust for the potential calculated deviance of the RLFNN. Asymptotical stability is assured by using the Lyapunov stability method, which generates the RLFNN's online learning algorithms. This study concludes that certain experimental results verify the effective and robust qualities of the suggested ICTCRLFNN controlled PMASynRM drive.

INDEX TERMS Permanent-magnet assisted synchronous reluctance motor (PMASynRM), computed torque control (CTC), intelligent computed torque control using recurrent Legendre fuzzy neural network (ICTCRLFNN), maximum torque per ampere (MTPA).

I. INTRODUCTION

Owing to rare-earth permanent magnets (PMs) being mounted on the rotor, the Interior permanent magnet synchronous motor (IPMSM) have a high torque and power density, wide speed operating range, and high efficiency. Therefore, they are widely used in electric vehicles (EVs) and vehicular applications [1], [2], [3], [4], such as starters/alternators, traction motor, power steering, and air conditioning motors. However, the rare-earth elements such as NdFeB are more expensive, and the monopoly of supply chain and trade war are two big concerns. Moreover, the disadvantages such as operated at the flux-weakening control region with large direct axis current and the uncontrolled generator mode caused by the permanent-magnet produced flux linkages are the restricting factors of high performance applications. Thus, a rather new machine called permanent-magnet assisted synchronous reluctance motor (PMASynRM) has been designed by reducing the amount of rare-earth PMs or using ferrite magnets in the

The associate editor coordinating the review of this manuscript and approving it for publication was Feifei Bu.

rotor to alleviate such difficulties [5]. Since the amount of rare-earth PMs and the resulted magnet flux linkages of the PMASynRM are rather small comparing with the conventional IPMSM, the reluctance torque becomes dominant in the developed torque. Furthermore, the PMASynRM can offer better power factor, torque capability and efficiency with respect to the synchronous reluctance motor (SynRM) [6], [7], [8].

Since the maximum torque per ampere (MTPA) control can improve the torque output in the constant torque region of the IPMSMs, some methods of MTPA have been published in recent years [9], [10], [11], [12], [13]. The MTPA is a control technique to reduce the copper losses by producing the required torque using the minimum current magnitude, which helps. A MTPA control using a saliency back-electromotive force-based intelligent torque observer was proposed in [9] for the improvement of speed estimating performance of a sensorless IPMSM drive system. In [10], a fuzzy control system, which adopted high-frequency mechanical power variation information, was developed to obtain the advance angle for a MTPA controlled IPMSM. Moreover, a small virtual current angle signal was injected in [11] to produce the d-axis current demand as well as to follow the MTPA operation point. In [12], a novel MTPA algorithm was proposed without using any motor dynamics and parameters, in which the current phase is varied continuously to minimize the magnitude of stator current vector at the given load torque. Furthermore, a machine learning approach was used to design the MTPA and flux-weakening control for an IPMSM in [13]. In addition, there are already some research for the MTPA controlled PMASynRM drive to improve its control characteristics in the constant torque region [14], [15]. However, the stator resistance and PM flux linkage are varying with motor temperature [15] and the d-q axis inductances are much influenced by the operating conditions of the motor drives.

The proportion-integral (PI) controller has been adopted in many control applications due to its simplicity. However, the disadvantages, such as sensitive to parameter variations and external disturbances, of the PI controller is well known. On the other hand, the computed torque control (CTC), which is designed by using Lyapunov stability theory [16], [17] has attracted great amount of attention for the nonlinear feedback control. The CTC is utilized to linearize the nonlinear equation of controlled plant by cancellation of some nonlinear terms [17]. Nevertheless, the objection to the real-time use of such control scheme is the lack of knowledge of the detailed system dynamics of the controlled plant. The intelligent control system by using fuzzy systems or neural networks can solve the above difficulty. Moreover, in various neural networks, the Legendre neural network (LNN), which adopts Legendre orthogonal polynomials, can effectively expand the input vector with nonlinear transformations [18], [19], [20]. When compares with the other orthogonal polynomials, the Legendre polynomial offers much less computational complexity than the functional link neural network using the trigonometric function [20]. Hence, LNN can effectively increase the dimensionality of the input vector with lower computational burden and faster convergence rate. Furthermore, by using varied functions to construct the consequent part in the fuzzy neural networks (FNNs) [21] can improve system performance [22], [23]. In [23], since the nonlinear and time-varying control characteristics of a synchronous reluctance motor (SynRM) limited the high-performance applications of this motor, an intelligent backstepping control using recurrent feature selection fuzzy neural network was proposed to construct a robust position controller for a SynRM servo drive system. Nevertheless, an LNN is added in the consequent part of the recurrent fuzzy neural network (RFNN) [24] to form a recurrent Legendre fuzzy neural network (RLFNN) to enhance the control and approximation performance by using the nonlinear combination of input variables in this study. Comparing with a fuzzy neural network (FNN), a recurrent Legendre fuzzy neural network (RLFNN) has several advantages. Firstly, RLFNN is capable of capturing the temporal characteristics of the system, making it well-suited for time-series prediction and control tasks. Secondly, RLFNN has a more flexible architecture, allowing for the use of multiple inputs and outputs, as well as the incorporation of recurrent connections that enable memory and feedback. This makes RLFNN more powerful in handling complex and dynamic systems with nonlinearities and uncertainties.

The main objective of this study is to build a high performance PMASynRM drive to achieve high energy efficiency and robust speed control simultaneously by using the MTPA and intelligent controls. In order to find the optimal current angle to maximize the output torque for a given stator current, the MTPA control has been widely adopted for the control of IPMSMs and SynRMs. Therefore, the copper loss can be minimized. On the other hand, the high-performance uses of the PMASynRM are constrained by the nonlinear and time-varying control elements of this motor even though it is of resilient composition, highly efficient, and inexpensive. Therefore, a Maxwell 2D simulation tool was adopted to assist the design of the PMASynRM to reach the necessary function in [25]. Moreover, this study aims to create an intelligent computed torque control (CTC) by operating the speed of a PMASynRM drive through the utilization of a recurrent Legendre fuzzy neural network (ICTCRLFNN) to achieve the robust control. In order to achieve optimal MTPA control, knowledge of the motor parameters is crucial. To address this issue, the team proposes an MTPA operated PMASynRM model that utilizes ANSYS Maxwell-2D. The current angle command for MTPA is generated by a lookup table (LUT), which is derived from the results of the finite element analysis (FEA). However, the process used to create the PMASynRM drive involves the introduction of various factors such as parameter variations, external disturbance, and lumped uncertainty, which can impact its properties. To mitigate these effects, the team employs a speed control method using a computed torque control (CTC). However,

applying CTC in practical situations can be challenging due to the unpredictable system dynamics inherent in the PMASynRM drive system. To address this challenge, the team proposes the use of a recurrent Legendre fuzzy neural network (RLFNN) as an approximation of the CTC. In addition, the team augments an adaptive compensator to adjust for the potential approximated deviance of the RLFNN. The Lyapunov stability method generates the RLFNN's online learning algorithms, which guarantees the robust control performance. In the end, a digital signal processor (DSP) TMS320F28075 with 32-bit floating point powers the PMASynRM drive's vector mechanism and suggested intelligent control system. Additionally, the major contributions of this study are: 1) The successful implementation of a high-performance PMASynRM speed drive with FEA-based MTPA in a 32-bit floating point DSP. 2) The successful development of an ICTCRLFNN and an adaptive compensator for the high-performance PMASynRM speed drive. 3) The successful derivation of a learning algorithm for the online training of the RLFNN using the Lyapunov stability theorem.

II. MODELLING OF PMASYNRM DRIVE SYSTEM

Owing to the high magnetic saturation of PMASynRMs under heavy loads, which will induce nonlinear torque generation, the FEA software such as Ansys Maxwell or JMAG is usually adopted for the design and analysis of PMASynRMs. Moreover, through the analysis of the motor mechanical design tool of ANSYS Maxwell-2D by using FEA, the current angle between the stator current and the MTPA can be obtained. Furthermore, the resulted minimum currents under various load torque conditions by using FEA are made into lookup table (LUT) to generate the current angle command of the MTPA. The cutaway of the adopted PMASynRM is shown in the Fig. 1. In addition, the designed parameters shown in Table 1 are used in developing the 2D FEA model of PMASynRM. To highlight the importance of considering magnetic saturation by using the parameters of PMASynRM shown in Table 2, Fig. 2 shows the relationship between the torque and current angle at various stator current magnitudes, where the red dotted line is the traditional maximum torque per ampere (TMTPA) trajectory without considering the magnetic saturation phenomenon; the black dotted line is the MTPA trajectory considering the magnetic saturation, which is the simulated results using Maxwell-2D. It can be found that the required stator current considering the magnetic saturation by using the MTPA is lower under the same torque.

The voltage equations of the stator of PMASynRM in the d-q reference frame can be expressed as follows:

$$v_d = R_s i_d + \frac{d}{dt}\lambda_d - \omega_e \lambda_q \tag{1}$$

$$v_q = R_s i_q + \frac{d}{dt}\lambda_q + \omega_e \lambda_d \tag{2}$$

TABLE 1. Model design parameters of PMASynRM.

Parameter	Quantities
Number of pole	4 pole
Number of slot	36 slot
Air gap length	0.3 mm
Inner diameter of rotor	31 mm
Outer diameter of rotor	94.4 mm
Inner diameter of stator	95 mm
Outer diameter of stator	160 mm
Stack length	150 mm

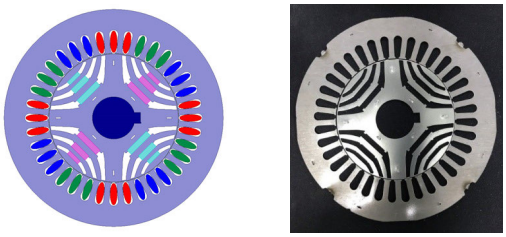

FIGURE 1. Cutaway of the PMASynRM.

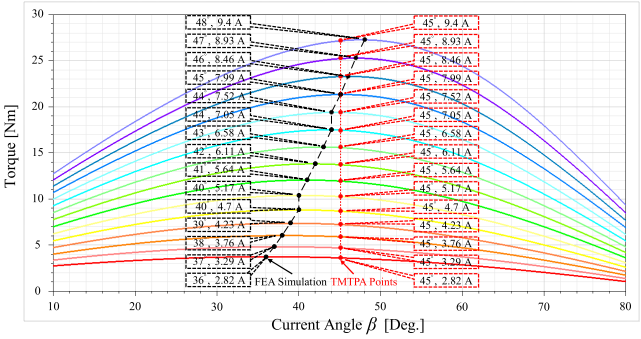

FIGURE 2. Torque versus current angle at various stator current magnitudes by using TMTPA control and MTPA control.

In (1) and (2), R_s is the stator resistance; v_d and v_q are the d-axis and q-axis voltage; i_d and i_q are the d-axis and q-axis stator currents; λ_d and λ_q are the d-axis and q-axis flux linkages; ω_e is the rotor electrical angular velocity. Moreover, the flux linkage equations in the d-q reference frame are:

$$\lambda_q = L_q i_q \tag{3}$$

$$\lambda_d = L_d i_d + \lambda_m \tag{4}$$

In the above equations, L_d and L_q are the d-axis and q-axis inductances; λ_m is the ferrite PM flux of the rotor. The produced electromagnetic torque of the PMASynRM without considering magnetic saturation expressed in the d-q reference frame can be expressed as follows:

$$T_e = \frac{3}{2}\frac{P}{2}[\lambda_m i_q + (L_d - L_q) i_q i_d] \tag{5}$$

and the number of pole is represented by P.

The control block diagram of PMASynRM drive system including the proposed CTC speed controller and ICTCRLFNN speed controller, current angle LUT, d-axis and q-axis PI current controllers and coordinate

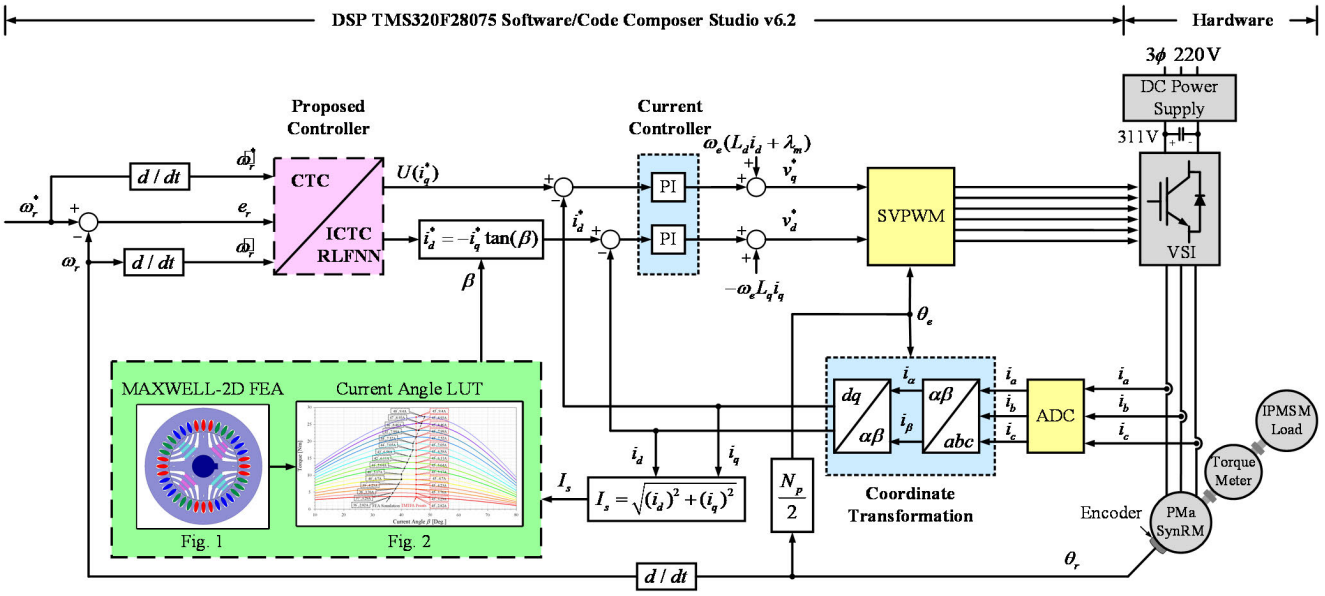

FIGURE 3. Control block diagram of PMASynRM speed drive system.

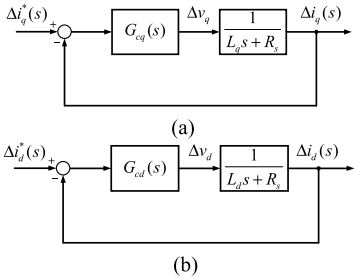

FIGURE 4. PI current controllers. (a) *q*-axis. (b) *d*-axis.

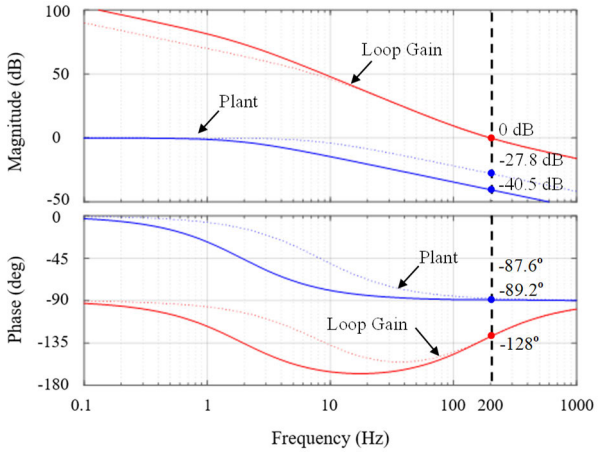

FIGURE 5. Bode diagrams of current controllers. Solid lines represent *q*-axis, and dashed lines represent *d*-axis.

transformation is shown in Fig. 3. The adopted PMASynRM is a 4 poles, 36 slots, 4.5 kW, 214 V, 9.4 A, 1500 rpm, 25 Nm type motor. In Fig. 3, ω_r^* is the motor speed command; ω_r is the speed response; e_r is the speed error; i_q^* is the q-axis current command; i_d^* is the d-axis current command; i_a, i_b, and i_c are the three phase currents. v_d^* is the d-axis voltage command; v_q^* is the q-axis voltage command. The command voltages v_a^*, v_b^*, and v_c^* are obtained by using the PI current controllers with voltage compensation terms and coordinate transformations as shown in Fig. 3. The three phase currents and are measured by using the Hall current sensors with 1 V/6.67 A transformation ratio and via the analog-to-digital converter (ADC). The space vector pulse width modulation (SVPWM) technology is implemented to control a voltage source inverter (VSI) also shown in Fig. 3. The switching frequency of the VSI is 20 kHz. In addition, silicon carbide (SiC) power MOSFET C3M0065090D manufactured by CREE with 900 V/36 A are adopted in the VSI.

The current controllers in this article are implemented by the PI controllers. The small signal models of the controlled plants for the design of q-d axis current controllers, which are shown in Figs. 4(a) and 4(b) respectively, can be represented by:

$$T_q(s) = \frac{1}{L_q s + R_s}, \quad T_d(s) = \frac{1}{L_d s + R_s} \tag{6}$$

where Δ represents small signal; s is the Laplace operator. Moreover, the PI current controllers are in the following forms:

$$G_{cq}(s) = K_p + \frac{K_i}{s}, \quad G_{cd}(s) = K_p + \frac{K_i}{s} \tag{7}$$

The bode diagrams of the controlled plants are shown in Fig. 5 in blue. The design specification of the current controller is bandwidth (BW) $f = 200$ Hz, phase margin (PM) $\phi_m = 52°$. It can be seen from Fig. 5 that the controlled plants needs to be compensated by 40.5 dB and $-38.8°$ and 27.8 dB and $-40.4°$, respectively, by using the q-d axis PI current

TABLE 2. Parameters of PMASynRM drive system.

Parameters	Quantities
Rated power	4.5 kW
Rated phase voltage	214 V
Rated phase current	9.4 Arms (delta)
Pole	4 pole
Slot number	36 slot
Rated speed	1500 rpm
Rated torque	25 Nm
d-axis inductance	19.6 mH
q-axis inductance	84.3 mH
Stator resistance	1.01Ω
Inertia coefficient	0.0069 Nm/(rad/sec^2)
Damping coefficient	0.0013 Nm/(rad/sec)
Magnetic flux	0.0854 Wb
DC-link	311 V
Sampling interval of current loop/ speed loop	0.1 ms/ 1 ms
Switching frequency	10 kHz
Encoder	TAMAGAWA incremental encoder: OIH 48-2500P4-L6-5V 2500 counts/turn

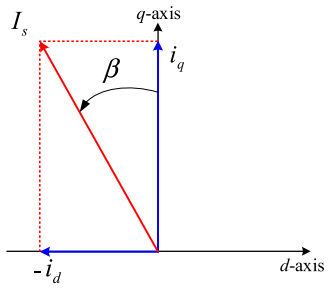

FIGURE 6. Relationship between the current vector I_s and the d-q.

controllers according to the parameters in Table 2. The resulted current controller is:

$$G_{cq}(s) = 82.55 + \frac{83407}{s}, \quad G_{cd}(s) = 18.69 + \frac{19992.34}{s} \tag{8}$$

The resulted bode diagrams of the loop gain are also shown in Fig. 5 in red. In addition, in the control block diagram shown in Fig. 3, the feedforward terms derived in (1) and (2), $\omega_e(L_d i_d + \lambda_m)$ and $-\omega_e L_q i_q$, are used for the decoupling control to let the current controllers be independent on speed ideally.

III. REALIZATION OF MTPA CONTROL

The output torque of the PMASynRM is composed of the electromagnetic torque of $\lambda_m i_q$ and the reluctance torque of $(L_d - L_q) i_q i_d$, respectively, and the reluctance torque is determined by the d-axis inductance and the q-axis inductance. Fig. 6 is the relationship between the stator current vector $\vec{I}_s$ and the d-q axis, in which $i_q = I_s \cos(\beta)$, $i_d = -I_s \sin(\beta)$. If the output torque is represented by the resultant current vector I_s, then:

$$T_e = \frac{3}{2}\frac{P}{2}[\lambda_m I_s \cos(\beta) + (L_d - L_q) I_s^2 \sin(2\beta)] \tag{9}$$

where β is the current angle. The current vector should be found for its magnitude to be as low as possible at a specific torque in order to operate the PMASynRM at the MTPA condition. Thus, the differentiation of the torque with respect to the current angle β in the synchronous reference frame depicts as follows [26]:

$$\frac{\partial T_e}{\partial \theta_i} = 2(L_d - L_q) I_s^2 \sin^2(\beta) \lambda_m I_s \sin(\beta) - (L_d - L_q) I_s^2 \tag{10}$$

Furthermore, the equation below provides the MTPA operation point and the resulted current angle β [15]:

$$\beta_{MTPA} = \sin^{-1}\left(\frac{-\lambda_m + \sqrt{\lambda_m^2 + 8(L_d - L_q)^2 I_s^2}}{-4(L_d - L_q) I_s}\right) \tag{11}$$

Based on (11), the optimal MTPA control only can be reached when there are clear motor parameters of L_d, L_q and λ_m. Despite this, the motor parameters still contain time-varying properties due to the motor's age, magnetic saturation, and operating temperature. Thus, solely utilizing (11) in real-world circumstances makes reaching MTPA control very complex. The team brings ANSYS Maxwell-2D into play in order to examine the MTPA's minimum current solution while taking in account for the PMASynRM's magnetic saturation properties. Finally, Fig. 3 depicts the MTPA's current angle command, which is generated by an LUT made from the results of the finite element analysis (FEA).

IV. DESIGN OF CTC AND ICTCRLFNN

Three challenges of this study are: (1) the design of an optimal MTPA control, which has been proposed in the previous section by using a FEA-based LUT; (2) the design of a robust speed control using intelligent control; (3) the development of a reliable online learning algorithm for the intelligent control to guarantee the stability. The last two challenges will be overcome by the proposed ICTCRLFNN in this section.

A. DESIGN OF CTC

The mechanical dynamic equation of the PMASynRM is

$$T_e = J\frac{d\omega_r}{dt} + B\omega_r + T_L \tag{12}$$

The ideal dynamic equation can use (5) and (12) to rewrite as follow:

$$\begin{aligned}\dot{\omega}_r &= -\frac{\bar{B}}{\bar{J}}\omega_r + \frac{3P[\bar{\lambda}_m + (\bar{L}_d - \bar{L}_q) i_d^*]}{4\bar{J}} i_q^* - \frac{T_L}{\bar{J}} \\ &= A_m \omega_r + B_m i_q^* + C_m T_L\end{aligned} \tag{13}$$

where $A_m = -\frac{\bar{B}}{\bar{J}}$; $B_m = \frac{3P[\bar{\lambda}_m + (\bar{L}_d - \bar{L}_q) i_d^*]}{4\bar{J}}$; $C_m = -\frac{1}{\bar{J}}$;
"$-$" represents the nominal value of the motor parameter.

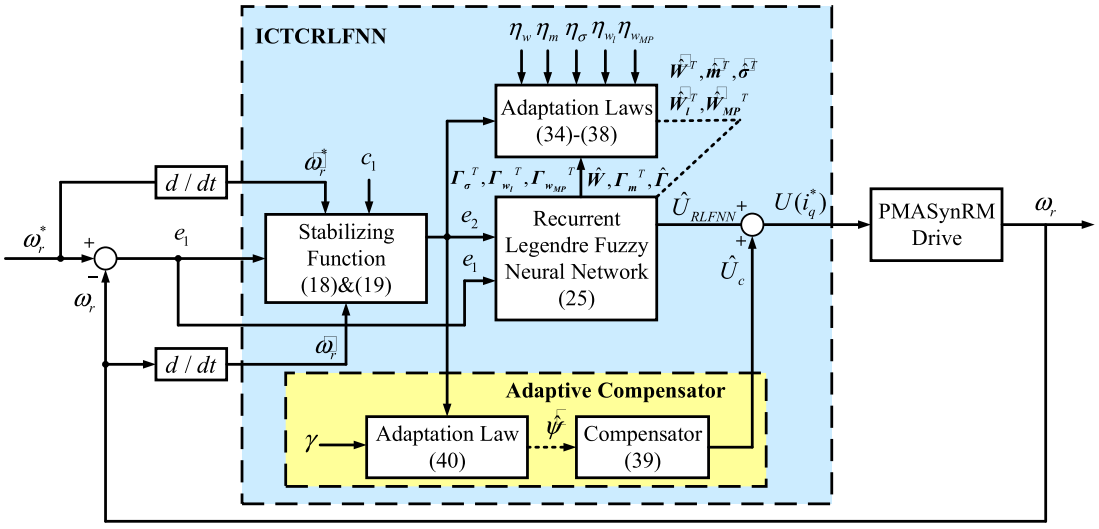

FIGURE 7. Control block diagram of PMASynRM speed drive using ICTCRLFNN.

With the consideration of the uncertainties, which includes parameter variations and external disturbance, the dynamic equation (13) can be rewritten as follow:

$$\begin{aligned}\dot{\omega}_r &= (A_m + \Delta A_m)\omega_r + (B_m + \Delta B_m)U + (C_m + \Delta C_m)T_L \\ &= A_m\omega_r + B_m U + F \end{aligned} \tag{14}$$

where $U = i_q^*$ is the torque current command. $C_m = -\frac{1}{J}$; ΔA_m, ΔB_m and ΔC_m denote the time-varying parameter variations; F is named the lumped uncertainty and defined by

$$F = \Delta A_m\omega_r + \Delta B_m U + (C_m + \Delta C_m)T_L, |F| \le F_b \tag{15}$$

and F_b represents the lumped uncertainty bound. Define the speed tracking error and its derivative as follows:

$$e_1 = \omega_r^*(t) - \omega_r(t) \tag{16}$$

$$\dot{e}_1 = \dot{\omega}_r^*(t) - \dot{\omega}_r(t) \tag{17}$$

$$\lambda_1 = -c_1 e_1 - \dot{\omega}_r^*(t) \tag{18}$$

and c_1 is a positive constant. Additionally, a virtual control error is defined:

$$e_2 = \dot{\omega}_r(t) + \lambda_1 = \dot{\omega}_r(t) - c_1 e_1 - \dot{\omega}_r^*(t) \tag{19}$$

Moreover, a Lyapunov function candidate is considered as:

$$V_1 = \frac{1}{2}e_1^2 + \frac{\left|\tilde{F}\right|^2}{2a} = \frac{1}{2}e_1^2 + \frac{\left|F - \hat{F}\right|^2}{2a} > 0 \tag{20}$$

with V_1 being a positive definite function; $\tilde{F} = F - \hat{F}$, $\hat{F}$ is the estimated value of F; a is a positive constant. Then, the derivative of V_1 can be derived as:

$$\begin{aligned}\dot{V}_1 &= e_1\dot{e}_1 - \frac{1}{a}\tilde{F}\dot{\hat{F}} = e_1(\dot{\omega}_r^* - \dot{\omega}_r) - \frac{1}{a}\tilde{F}\dot{\hat{F}} \\ &= e_1(-c_1 e_1 - e_2) - \frac{1}{a}\tilde{F}\dot{\hat{F}} \\ &= -c_1 e_1^2 - (\omega_r^* - \omega_r)e_2 - \frac{1}{a}\tilde{F}\dot{\hat{F}} \\ &= -c_1 e_1^2 - [\omega_r^* - \frac{1}{A_m}(\dot{\omega}_r - B_m U - F)]e_2 - \frac{1}{a}\tilde{F}\dot{\hat{F}} \\ &= -c_1 e_1^2 - (\omega_r^* - \frac{1}{A_m}\dot{\omega}_r + \frac{1}{A_m}B_m U + \frac{1}{A_m}\hat{F})e_2 \\ &\quad - \frac{\tilde{F}}{a}(\frac{ae_2}{A_m} + \dot{\hat{F}}) \end{aligned} \tag{21}$$

According to $\dot{V}_1$, an CTC law U and adaptive law $\dot{\hat{F}}$ [16], [17] are designed as follows:

$$U_{CTC} = i_q^* = B_m^{-1}(-A_m\omega_r^* + A_m c_2 e_2 + \dot{\omega}_r - \hat{F}) \tag{22}$$

$$\dot{\hat{F}} = -\frac{ae_2}{A_m} \tag{23}$$

Substituting (22), (23) into (21), the following equation can be obtained:

$$\dot{V}_1 = -c_1 e_1^2 - c_2 e_2^2 \le 0 \tag{24}$$

indicating that e_1 and e_2 will converge to zero as $t \to \infty$. As the result, the CTC speed control is asymptotically stable. Though the CTC system can guarantee the asymptotically stability of PMASynRM drive system, the lumped uncertainty F is unknown in practical applications. However, the CTC system requires the actual parameters of the PMASynRM drive system in advance. In addition, the slow adaptation of the lumped uncertainty shown in (23) resulted in sluggish dynamical response. Thus, it is unfeasible to design a CTC law for practical applications.

B. DESIGN OF ICTCRLFNN

A RLFNN controller is proposed to approximate the CTC law shown in (22) to overcome the above shortcomings of the CTC as shown in Fig. 7. Moreover, the control law for the ICTCRLFNN system is designed as follow:

$$U = \hat{U}_{RLFNN} + \hat{U}_c \tag{25}$$

In the above equation, $\hat{U}_{RLFNN}$ is designed to learn the CTC law and $\hat{U}_c$ is used to compensate the approximated error of the RLFNN controller. The six-layer RLFNN shown in Fig. 8 can be represented in the following form:

$$\begin{aligned}
&U_{RLFNN}(e_1, e_2, \boldsymbol{W}, \boldsymbol{W_l}, \boldsymbol{W_{MP}}, \boldsymbol{m}, \boldsymbol{\sigma}) \equiv \boldsymbol{W\Gamma} \\
&\boldsymbol{W} = [w_1^6\ w_2^6\ w_3^6\ w_4^6\ w_5^6\ w_6^6\ w_7^6\ w_8^6\ w_9^6] \in R^{1\times 9}; \\
&\boldsymbol{\Gamma} = [x_1^6\ x_2^6\ x_3^6 x_4^6\ x_5^6\ x_6^6\ x_7^6\ x_8^6\ x_9^6]^T \in R^{9\times 1}; \\
&\boldsymbol{W_l} = [w_1^4\ w_2^4\ w_3^4\ w_4^4\ w_5^4\ w_6^4\ w_7^4\ w_8^4\ w_9^4]^T \in R^{9\times 1}; \\
&\boldsymbol{W_{MP}} = [w_1^3\ w_2^3\ \cdots w_{81}^3\ ]^T \in R^{81\times 1}; \\
&\boldsymbol{m} = [m_{11}\ m_{12}\ m_{13}\ m_{24}\ m_{25}\ m_{26}]^T \in R^{6\times 1}; \\
&\boldsymbol{\sigma} = [\sigma_{11}\ \sigma_{12}\ \sigma_{13}\ \sigma_{24}\ \sigma_{25}\ \sigma_{26}]^T \in R^{6\times 1}; \qquad (26)
\end{aligned}$$

In (26), $\boldsymbol{m}$ and $\boldsymbol{\sigma}$ are the vector of mean and the standard deviation of the Gaussian functions in Layer 2. There is an optimal U^*_{RLFNN} for any nonlinear function according to the universal approximation property. Thus, an optimal U^*_{RLFNN} is designed to learn the CTC law U_{CTC} such that

$$\begin{aligned}
U_{CTC} &= U^*_{RLFNN}(e_1, e_2, \boldsymbol{W}^*, \boldsymbol{W}^*_{\boldsymbol{l}}, \boldsymbol{W}^*_{\boldsymbol{MP}}, \boldsymbol{m}^*, \boldsymbol{\sigma}^*) + \varepsilon \\
&= \boldsymbol{W}^*\boldsymbol{\Gamma}^* + \varepsilon \qquad (27)
\end{aligned}$$

In (27), ε is the minimum reconstructed error; $\boldsymbol{W}^*$, $\boldsymbol{W}^*_{\boldsymbol{l}}$, $\boldsymbol{W}^*_{\boldsymbol{MP}}$, $\boldsymbol{m}^*$, $\boldsymbol{\sigma}^*$ and $\boldsymbol{\Gamma}^*$ are the optimal values of $\boldsymbol{W}$, $\boldsymbol{W_l}$, $\boldsymbol{W_{MP}}$, $\boldsymbol{m}$, $\boldsymbol{\sigma}$ and $\boldsymbol{\Gamma}$ respectively. Furthermore, the control law shown in (25) can be represented as:

$$U = \hat{U}_{RLFNN}(e_1, e_2, \hat{\boldsymbol{W}}, \hat{\boldsymbol{W}}_{\boldsymbol{l}}, \hat{\boldsymbol{W}}_{\boldsymbol{MP}}, \hat{\boldsymbol{m}}, \hat{\boldsymbol{\sigma}}) + \hat{U}_c = \hat{\boldsymbol{W}}\hat{\boldsymbol{\Gamma}} + \hat{U}_c \qquad (28)$$

In (28), $\hat{\boldsymbol{W}}$, $\hat{\boldsymbol{W}}_{\boldsymbol{l}}$, $\hat{\boldsymbol{W}}_{\boldsymbol{MP}}$, $\hat{\boldsymbol{m}}$, and $\hat{\boldsymbol{\sigma}}$ are the estimated values of $\boldsymbol{W}$, $\boldsymbol{W_l}$, $\boldsymbol{W_{MP}}$, $\boldsymbol{m}$ and $\boldsymbol{\sigma}$. Subtracting (28) from (27), the following equation can be obtained:

$$\tilde{U} = U_{CTC} - U = \tilde{\boldsymbol{W}}\boldsymbol{\Gamma}^* + \hat{\boldsymbol{W}}\tilde{\boldsymbol{\Gamma}} + \varepsilon - \hat{U}_c \qquad (29)$$

and $\tilde{\boldsymbol{W}} = \boldsymbol{W}^* - \hat{\boldsymbol{W}}$, $\tilde{\boldsymbol{\Gamma}} = \boldsymbol{\Gamma}^* - \hat{\boldsymbol{\Gamma}}$. In order to transform the nonlinear RLFNN into partially linear form, a linearization technique is applied to obtain the expansion of $\tilde{\boldsymbol{\Gamma}}$ in Taylor series as follows:

$$\tilde{\boldsymbol{\Gamma}} = \boldsymbol{\Gamma}^T_{\boldsymbol{m}}\tilde{\boldsymbol{m}} + \boldsymbol{\Gamma}^T_{\boldsymbol{\sigma}}\tilde{\boldsymbol{\sigma}} + \boldsymbol{\Gamma}^T_{\boldsymbol{w_l}}\tilde{\boldsymbol{W}}_{\boldsymbol{l}} + \boldsymbol{\Gamma}^T_{\boldsymbol{w_{MP}}}\tilde{\boldsymbol{W}}_{\boldsymbol{MP}} + N_h \qquad (30)$$

In (30), $\tilde{\boldsymbol{m}} = \boldsymbol{m}^* - \hat{\boldsymbol{m}}$, $\tilde{\boldsymbol{\sigma}} = \boldsymbol{\sigma}^* - \hat{\boldsymbol{\sigma}}$, $\tilde{\boldsymbol{W}}_{\boldsymbol{l}} = \boldsymbol{W}^*_{\boldsymbol{l}} - \hat{\boldsymbol{W}}_{\boldsymbol{l}}$, $\tilde{\boldsymbol{W}}_{\boldsymbol{MP}} = \boldsymbol{W}^*_{\boldsymbol{MP}} - \hat{\boldsymbol{W}}_{\boldsymbol{MP}}$; N_h represents the high-order term. In addition,

$$\boldsymbol{\Gamma}^T_{\boldsymbol{m}} = \begin{bmatrix} \frac{\partial x_1^6}{\partial m_{11}} & \frac{\partial x_1^6}{\partial m_{12}} & \cdots & \frac{\partial x_1^6}{\partial m_{26}} \\ \frac{\partial x_2^6}{\partial m_{11}} & \frac{\partial x_2^6}{\partial m_{12}} & \cdots & \frac{\partial x_2^6}{\partial m_{26}} \\ \vdots & \vdots & \ddots & \vdots \\ \frac{\partial x_9^6}{\partial m_{11}} & \frac{\partial x_9^6}{\partial m_{12}} & \cdots & \frac{\partial x_9^6}{\partial m_{26}} \end{bmatrix} R^{9\times 6}$$

$$\boldsymbol{\Gamma}^T_{\sigma} = \begin{bmatrix} \frac{\partial x_1^6}{\partial \sigma_{11}} & \frac{\partial x_1^6}{\partial \sigma_{12}} & \cdots & \frac{\partial x_1^6}{\partial \sigma_{26}} \\ \frac{\partial x_2^6}{\partial \sigma_{11}} & \frac{\partial x_2^6}{\partial \sigma_{12}} & \cdots & \frac{\partial x_2^6}{\partial \sigma_{26}} \\ \vdots & \vdots & \ddots & \vdots \\ \frac{\partial x_9^6}{\partial \sigma_{11}} & \frac{\partial x_9^6}{\partial \sigma_{12}} & \cdots & \frac{\partial x_9^6}{\partial \sigma_{26}} \end{bmatrix} \in R^{9\times 6}$$

$$\boldsymbol{\Gamma}^T_{W_l} = \begin{bmatrix} \frac{\partial x_1^6}{\partial w_1^4} & \frac{\partial x_1^6}{\partial w_2^4} & \cdots & \frac{\partial x_1^6}{\partial w_9^4} \\ \frac{\partial x_2^6}{\partial w_1^4} & \frac{\partial x_2^6}{\partial w_2^4} & \cdots & \frac{\partial x_2^6}{\partial w_9^4} \\ \vdots & \vdots & \ddots & \vdots \\ \frac{\partial x_9^6}{\partial w_1^4} & \frac{\partial x_9^6}{\partial w_2^4} & \cdots & \frac{\partial x_9^6}{\partial w_9^4} \end{bmatrix} \in R^{9\times 6}$$

$$\boldsymbol{\Gamma}^T_{W_{MP}} = \begin{bmatrix} \frac{\partial x_1^6}{\partial w_{11}^3} & \frac{\partial x_1^6}{\partial w_{12}^3} & \cdots & \frac{\partial x_1^6}{\partial w_{99}^3} \\ \frac{\partial x_2^6}{\partial w_{11}^3} & \frac{\partial x_2^6}{\partial w_{12}^3} & \cdots & \frac{\partial x_2^6}{\partial w_{99}^3} \\ \vdots & \vdots & \ddots & \vdots \\ \frac{\partial x_9^6}{\partial w_{11}^3} & \frac{\partial x_9^6}{\partial w_{12}^3} & \cdots & \frac{\partial x_9^6}{\partial w_{99}^3} \end{bmatrix} \in R^{9\times 81}$$

Rewriting (30), $\boldsymbol{\Gamma}^*$ can be obtained that

$$\boldsymbol{\Gamma}^* = \hat{\boldsymbol{\Gamma}} + \tilde{\boldsymbol{\Gamma}} = \hat{\boldsymbol{\Gamma}} + \boldsymbol{\Gamma}^T_{\boldsymbol{m}}\tilde{\boldsymbol{m}} + \boldsymbol{\Gamma}^T_{\boldsymbol{\sigma}}\tilde{\boldsymbol{\sigma}} + \boldsymbol{\Gamma}^T_{\boldsymbol{w_l}}\tilde{\boldsymbol{W}}_{\boldsymbol{l}} + \boldsymbol{\Gamma}^T_{\boldsymbol{w_{MP}}}\tilde{\boldsymbol{W}}_{\boldsymbol{MP}} + N_h \qquad (31)$$

Substituting (30) and (31) into (29), the estimated error in (29) can now be written as

$$\begin{aligned}
\tilde{U} &= \tilde{\boldsymbol{W}}\boldsymbol{\Gamma}^* + \hat{\boldsymbol{W}}\tilde{\boldsymbol{\Gamma}} + \varepsilon - \hat{U}_c \\
&= \tilde{\boldsymbol{W}}\hat{\boldsymbol{\Gamma}} + \hat{\boldsymbol{W}}\boldsymbol{\Gamma}^T_{\boldsymbol{m}}\tilde{\boldsymbol{m}} + \hat{\boldsymbol{W}}\boldsymbol{\Gamma}^T_{\boldsymbol{\sigma}}\tilde{\boldsymbol{\sigma}} + \hat{\boldsymbol{W}}\boldsymbol{\Gamma}^T_{\boldsymbol{w_l}}\tilde{\boldsymbol{W}}_{\boldsymbol{l}} \\
&\quad + \hat{\boldsymbol{W}}\boldsymbol{\Gamma}^T_{\boldsymbol{w_{MP}}}\tilde{\boldsymbol{W}}_{\boldsymbol{MP}} + H - \hat{U}_c \qquad (32)
\end{aligned}$$

and H represents the uncertain term and can be written as:

$$\begin{aligned}
H = \tilde{\boldsymbol{W}}\boldsymbol{\Gamma}^T_{\boldsymbol{m}}\tilde{\boldsymbol{m}} + \tilde{\boldsymbol{W}}\boldsymbol{\Gamma}^T_{\boldsymbol{\sigma}}\tilde{\boldsymbol{\sigma}} + \tilde{\boldsymbol{W}}\boldsymbol{\Gamma}^T_{\boldsymbol{w_l}}\tilde{\boldsymbol{W}}_{\boldsymbol{l}} + \tilde{\boldsymbol{W}}\boldsymbol{\Gamma}^T_{\boldsymbol{w_{MP}}}\tilde{\boldsymbol{W}}_{\boldsymbol{MP}} \\
+ \boldsymbol{W}^*N_h + \varepsilon \qquad (33)
\end{aligned}$$

Theorem 1: Taking account for the PMASynRM drive system, which is depicted in (14), the suggested ICTCRLFNN will acquire absolute asymptotical stability once the parameters below are achieved: 1) The ICTCRLFNN control is created as depicted in (25); 2) The RLFNN's adaptation law is created as depicted in (34)-(38); 3) The compensators equipped with an adaption law are created as depicted in (39) and (40).

$$\dot{\hat{\boldsymbol{W}}}^T = \eta_w e_2 \hat{\boldsymbol{\Gamma}} \qquad (34)$$

$$\dot{\hat{\boldsymbol{m}}}^T = \eta_m e_2 \hat{\boldsymbol{W}}\boldsymbol{\Gamma}^T_{\boldsymbol{m}} \qquad (35)$$

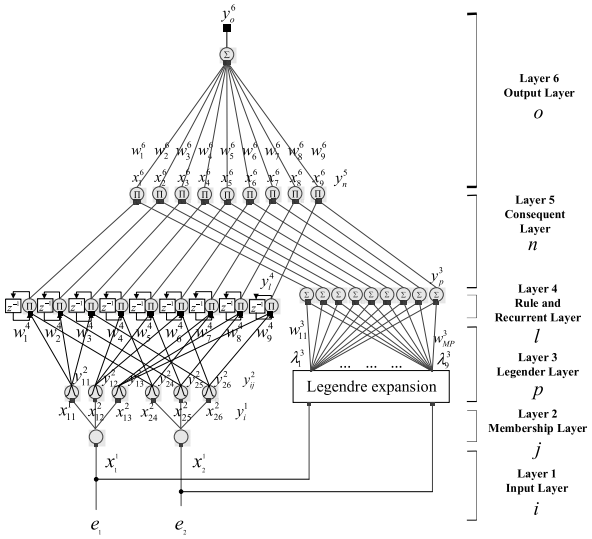

FIGURE 8. Network structure of RLFNN.

$$\dot{\hat{\sigma}}^T = \eta_\sigma e_2 \hat{W} \Gamma_\sigma^T \tag{36}$$

$$\dot{\hat{W}}_l^T = \eta_{w_l} e_2 \hat{W} \Gamma_{w_l}^T \tag{37}$$

$$\dot{\hat{W}}_{MP}^T = \eta_{w_{MP}} e_2 \hat{W} \Gamma_{w_{MP}}^T \tag{38}$$

$$\hat{U}_c = \hat{\psi} \tag{39}$$

$$\dot{\hat{\psi}} = \gamma e_2 \tag{40}$$

where η_w, η_m, η_σ, η_{w_l} and $\eta_{w_{MP}}$ are learning rates parameters and are all sets as positive constants; $\hat{\psi}$ is the online estimated value of approximated error; and γ is a positive constant.

Proof: Considering a Lyapunov function candidate as:

$$\begin{aligned} V_2(e_1(t), \tilde{\psi}(t), \tilde{W}, \tilde{W}_l, \tilde{W}_{MP}, \tilde{m}, \tilde{\sigma}) &= \frac{1}{2}e_1^2 + \frac{\left|\tilde{F}\right|^2}{2a} + \frac{B_m}{2A_m\eta_w}\tilde{W}\tilde{W}^T \\ &+ \frac{B_m}{2A_m\eta_{w_l}}\tilde{W}_l^T\tilde{W}_l + \frac{B_m}{2A_m\eta_{w_{MP}}}\tilde{W}_{MP}^T \\ &\times \tilde{W}_{MP} + \frac{B_m}{2A_m\eta_m}\tilde{m}^T\tilde{m} \\ &+ \frac{B_m}{2A_m\eta_\sigma}\tilde{\sigma}^T\tilde{\sigma} + \frac{B_m}{2A_m\gamma}\left\|\tilde{\psi}\right\|^2 > 0 \end{aligned} \tag{41}$$

where V_2 is a function of positive definite. Additionally, $\tilde{\psi} = \psi - \hat{\psi}$ is the approximated error and defined as:

$$\psi = H - \frac{\tilde{F}}{B_m} - \frac{1}{ae_2B_m}\tilde{F}\dot{\tilde{F}} \tag{42}$$

Then, differentiate V_2 with respect to time the following equation can be obtained:

$$\begin{aligned} \dot{V}_2 &= -c_1e_1^2 - c_2e_2^2 + [\frac{e_2B_m}{A_m}\tilde{W}\hat{\Gamma} - \frac{B_m}{A_m\eta_w}\tilde{W}\dot{\hat{W}}^T] \\ &+ [\frac{e_2B_m}{A_m}\hat{W}\Gamma_m^T\tilde{m} \\ &- \frac{B_m}{A_m\eta_m}\dot{\hat{m}}^T\tilde{m}] + [\frac{e_2B_m}{A_m}\hat{W}\Gamma_\sigma^T\tilde{\sigma} - \frac{B_m}{A_m\eta_\sigma}\dot{\hat{\sigma}}^T\tilde{\sigma}] \\ &+ [\frac{e_2B_m}{A_m}\hat{W}\Gamma_{w_l}^T\tilde{W}_l - \frac{B_m}{A_m\eta_{w_l}}\dot{\hat{W}}_l^T\tilde{W}_l] \\ &+ [\frac{e_2B_m}{A_m}\hat{W}\Gamma_{w_{MP}}^T\tilde{W}_{MP} \\ &- \frac{B_m}{A_m\eta_{w_{MP}}}\dot{\hat{W}}_{MP}^T\tilde{W}_{MP}] + \frac{e_2B_m}{A_m}(\hat{\psi} - \hat{U}_c) \\ &+ \frac{B_m}{A_m\gamma}\tilde{\psi}(\gamma e_2 - \dot{\hat{\psi}}) \end{aligned} \tag{43}$$

Moreover, substitute (34)–(40) into (43), it can be concluded that

$$\dot{V}_2(e_1(t), \tilde{\psi}(t), \tilde{W}, \tilde{W}_l, \tilde{W}_{MP}, \tilde{m}, \tilde{\sigma}) = -c_1e_1^2 - c_2e_2^2 \le 0 \tag{44}$$

Since $\dot{V}_2(e_1(t), \tilde{\psi}(t), \tilde{W}, \tilde{W}_l, \tilde{W}_{MP}, \tilde{m}, \tilde{\sigma}) \le 0$ is negative semidefinite, all signals contained in (41) are bounded. Furthermore, by using Barbalat's Lemma, it can be inferred that e_1, e_2 will converge to zero as $t \to \infty$. This complete the proof that the proposed ICTCRLFNN control system is asymptotically stable. Detailed derivation can be referred to [23].

The flowchart for the proposed RLFNN controller is shown in Fig. 9. The operating mechanism in the proposed RLFNN are described in detail as follows:

1. Sampling: An incremental encoder with resolution 2500 counts/rev is adopted to measure the rotor position by using the eQEP module in the DSP. Then, the derivative of rotor position ω_r is calculated. Following that, the tracking

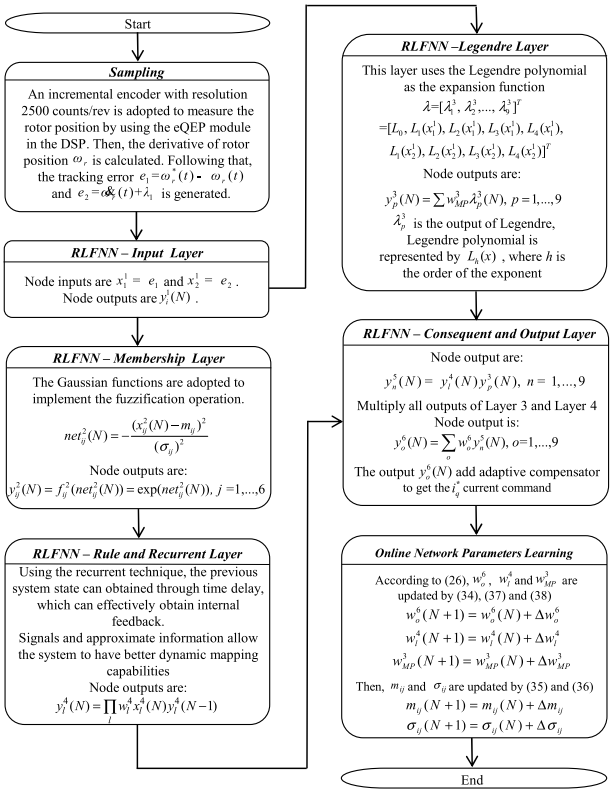

FIGURE 9. Flowchart of proposed RLFNN controller for speed control.

error $e_1 = \omega_r^*(t) - \omega_r(t)$ or $e_2 = \dot{\omega}_r(t) + \lambda_1$ is generated and sent to the proposed RLFNN controller.

2. RLFNN Input Layer: The input variables of the proposed FNN are $x_1^1 = e_1$ and $x_2^1 = e_2$. In the input layer, the node outputs are $y_i^1(N)$ and sent to the membership layer.

3. RLFNN Membership Layer: The Gaussian functions are adopted to implement the fuzzification operation and the outputs are $y_{ij}^2(N)$. Then, the outputs $y_{ij}^2(N)$ are sent to the rule and recurrent layer.

4. RLFNN Legendre Layer: This layer uses the Legendre polynomial as the expansion function, and its input variable vector $x = [x_1^1, x_2^1]$ can be divided into:

$$\begin{aligned}\lambda &= [\lambda_1^3, \lambda_2^3, \ldots, \lambda_9^3]^T \\ &= [L_0, L_1(x_1^1), L_2(x_1^1), L_3(x_1^1), L_4(x_1^1), L_1(x_2^1), \\ &\quad L_2(x_2^1), L_3(x_2^1), L_4(x_2^1)]^T\end{aligned}$$

Legendre polynomial is represented by $L_h(x)$, where h is the order of the exponent. In this layer, the node outputs $y_p^3(N)$ are obtained by performing the summation and multiplying operations with w_{MP}^3 and λ_P^3.

5. RLFNN Rule and Recurrent Layer: Using the recurrent technique, the previous system state can obtained through time delay, which can effectively obtain internal feedback. Signals and approximate information allow the system to have better dynamic mapping capabilities. Then, the outputs $y_l^4(N)$ are sent to the rule and recurrent layer.

6. RLFNN Consequent Layer: The nodes of consequent layer multiply the output signals from rule and recurrent layer, Legendre layer and recurrent property, and output the result of product for dynamic mapping. The outputs are $y_n^5(N)$ and sent to the output layer.

7. RLFNN Output Layer: The node performs the summation and multiplying operation. Then, the output is given as $y_o^6(N)$, which add adaptive compensator to get the i_q^* current command.

8. Online Network Parameters Learnings: The online parameters learning are achieved by online tuning of the connective weights w_o^6 in the output layer, the connective weights w_l^4 in the rule and recurrent layer, the connective weights w_{MP}^3 in the Legendre layer, and the mean m_{ij} and standard deviations σ_{ij} of the membership functions in the membership layer.

Though all the learning rate parameters and set as positive constants, too large positive constants will result in the divergence of the RLFNN, and too small positive constants will result in the slow convergence of the RLFNN. Therefore, the learning rate parameters are tuned by trial and error in the experimentation.

V. EXPERIMENTATION

Fig. 10 depicts the experimental setup, which encompasses the PMASynRM drive, torque meter, the DSP TMS320F28075 control board, input/output (I/O) extension board, encoder interface board, IPMSM load, and the personal computer for the development system. A controlled

TABLE 3. Test scenarios in experimentation.

Case	Controller	Speed command [r/min]	Load torque [Nm]	Figure
Case 1	CTC	500 + 100 periodical step	5 to 10	Figure 12. (a)
Case 2	CTC	1000 + 100 periodical step	5 to 10	Figure 12. (c)
Case 1	CTC	500+100$sin(t)$	5 to 10	Figure 13. (a)
Case 2	CTC	1000+100$sin(t)$	5 to 10	Figure 13. (c)
Case 1	ICTCRLFNN	500 + 100 periodical step	5 to 10	Figure 14. (a)
Case 2	ICTCRLFNN	1000 + 100 periodical step	5 to 10	Figure 14. (c)
Case 1	ICTCRLFNN	500+100$sin(t)$	5 to 10	Figure 15. (a)
Case 2	ICTCRLFNN	1000+100$sin(t)$	5 to 10	Figure 15. (c)

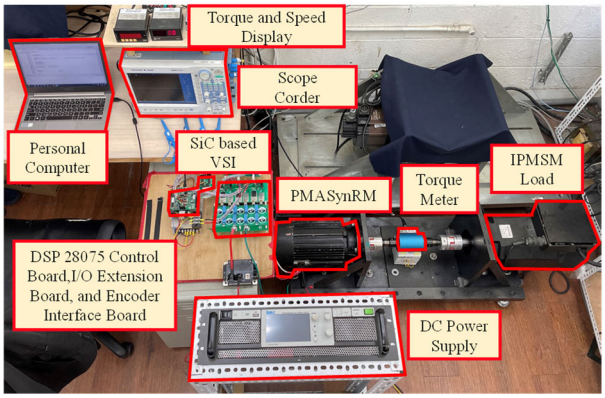

FIGURE 10. Photograph of experimental setup.

DC power supply powers the DC link of the 4.5 kW SiC based VSI. During the experiment, the team sets an industrial drive of the 7.5 kW IPMSM at torque control mode and 5 Nm and 10 Nm for load torque. An incremental encoder operated through a QEP interface featuring a 1 ms sampling rate ascertains the position of the PMASynRM. 0.1 ms serves as the current control loop's switching and sampling intervals. Subsequently, the PMASynRM drive is operated by the SVPWM's switching commands being delivered to the VSI.

T_M, T_{aver}, and T_{sd}, which are the maximum tracking error, the average tracking error, and the standard deviation of the tracking error [17], respectively, are adopted to verify the control performance within the suggested speed control system:

$$T_M = \max_N(|T_{error}(N)|) \tag{45}$$

$$T_{aver} = \frac{\sum_{N=1}^{h} |T_{error}(N)|}{h} \tag{46}$$

$$T_{sd} = \sqrt{\frac{\sum_{N=1}^{h} (T_{error}(N) - T_{aver}(N))^2}{h}} \tag{47}$$

where $T_{error}(N) = \omega_r^*(N) - \omega_r(N)$; h is the total number of iterations. The responses of periodical step and sinusoidal reference trajectories are measured to show the control system's control performance. The following second-order transfer function with rise time 0.6 s serves as the reference

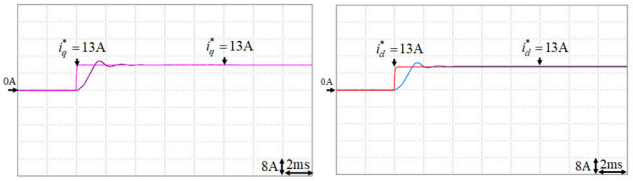

FIGURE 11. Current responses of *q-d* axis current control by using PI controllers. (a) Step command and response of *q*-axis current. (b) Step command and response of *d*-axis current.

model for the periodic step reference input:

$$\frac{\omega_n^2}{s^2 + 2\xi\omega_n s + \omega_n^2} = \frac{30}{s^2 + 11s + 30} \tag{48}$$

In (48), ξ and ω_n denote the damping ratio and undamped natural frequency, respectively. Moreover, the experimental results of CTC and proposed ICTCRLFNN speed controllers are provided and analyzed for the comparison of the control performance. The parameters of the CTC speed controller is designed using the motor parameters shown in Table 2. The parameters of the CTC and the proposed ICTCRLFNN speed controller are given in (49) and (50) as follows:

$$a = 1.5, \quad c_1 = 545, \; c_2 = 0.24$$
$$c_1 = 545, \quad \eta_w = 0.01, \; \eta_m = 0.175, \tag{49}$$
$$\eta_\sigma = 0.017, \quad \eta_{w_l} = 0.22, \; \eta_{w_{MP}} = 0.95, \; \gamma = 18 \tag{50}$$

The parameters are tuned by trial and error to achieve the best transient control performance with the consideration of the stability requirement. Though optimization algorithms, such as genetic algorithm and particle swarm optimization, can be used to search for the optimal set of parameter values that achieve the desired performance criteria, the disadvantage of the optimization algorithms is time consuming. Furthermore, to compromise between the computation amount and the control performance, two, six, nine, nine, nine and one neurons have been selected in the input, membership, Legendre, rule, consequent and output layer for the network structure of the RLFNN.

The control objective in the experimentation is to control the rotor speed of the PMASynRM to track the periodically speed commands with minimum tracking error including step (100 rpm) and sinusoidal (±100 rpm) commands. Some experimental results are provided to demonstrate the effectiveness of the proposed PMASynRM drive. First, the control performance of the current control is shown in Fig. 11. Figs. 11 (a) and 11(b) show the current responses of the *q-d* axis current control by using the designed PI controllers shown in (10) with step command where 13 A is the rated value of the phase current. Owing to the specification PM 52°, the overshoot of current step responses are both 13% as shown in Figs. 11(a) and 11(b). Then, two different operating points 500 rpm (case 1) and 1000 rpm (case 2) are presented where the load torque transiting from 5 Nm to 10 Nm at 10 s for the speed control. In order to test the parameter sensitivity and robustness of the proposed

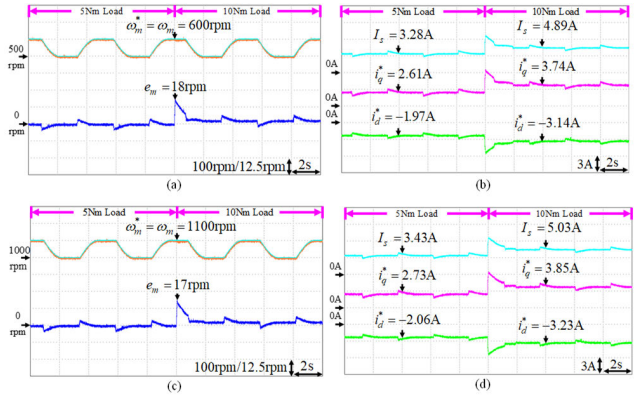

FIGURE 12. Results of CTC speed controller for periodical step command. (a) Rotor response and tracking error at case 1. (b) Stator and *d-q* axis current commands at case 1. (c) Rotor response and tracking error at case 2. (d) Stator and *d-q* axis current commands at case 2.

TABLE 4. Quantified comparison of experimental results.

Case	Controller	Speed command [r/min]	Maximum tracking error [r/min]	Transient time [sec]
Case 1	CTC	500 + 100 periodical step	18	0.88
Case 2	CTC	1000 + 100 periodical step	17	0.97
Case 1	CTC	500+100*sin*(*t*)	18	1.08
Case 2	CTC	1000+100*sin*(*t*)	16	1.1
Case 1	ICTCRLFNN	500 + 100 periodical step	14	0.77
Case 2	ICTCRLFNN	1000 + 100 periodical step	13	0.82
Case 1	ICTCRLFNN	500+100*sin*(*t*)	13	0.83
Case 2	ICTCRLFNN	1000+100*sin*(*t*)	12	0.91

controllers at different operating conditions, the test scenarios in the experimentation have been shown in Table 3. Figs. 12 and 13 depict the experimental results of the command tracking due to the periodical step and sinusoidal commands of CTC speed controller at case 1 and case 2. The rotor responses and tracking errors are shown in Figs. 12(a), 12(c), 13(a) and 13(c); the current commands are shown in Figs. 12(b), 12(d), 13(b) and 13(d). On the other hand, Figs. 14 and 15 depict the experimental results of the command tracking due to the periodical step and sinusoidal commands of the proposed ICTCRLFNN speed controller at case 1 and case 2. The rotor responses and tracking errors are shown in Figs. 14(a), 14(c), 15(a) and 15(c); the current commands are shown in Figs. 14(b), 14(d), 15(b) and 15(d). From the experimental results, the *d*-axis current command can be effectively generated by using the FEA-based LUT for the MTPA control. Additionally, comparing with CTC speed controller, the rotor responses of the PMASynRM using the proposed ICTCRLFNN speed controller are much enhanced and the tracking errors are reduced at different reference commands owing to the RLFNN with the capabilities of parallel processing and online learning of the network parameters. That is to say, the robustness of the speed control is improved by using the proposed ICTCRFNN speed controller. The results of all the experiments shown in Figs. 12 to 15 have been quantified and compared in Table 4.

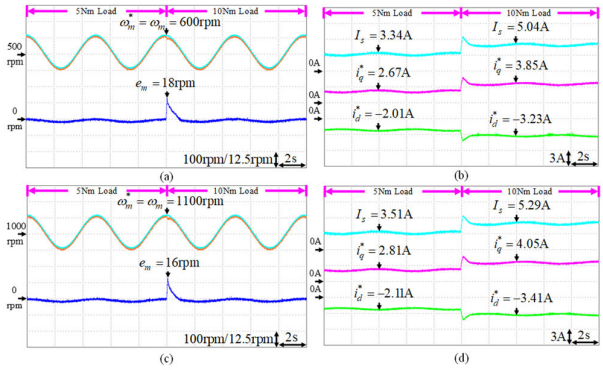

FIGURE 13. Results of CTC speed controller for periodical sinusoidal command. (a) Rotor response and tracking error at case 1. (b) Stator and *d*-*q* axis current commands at case 1. (c) Rotor response and tracking error at case 2. (d) Stator and *d*-*q* axis current commands at case 2.

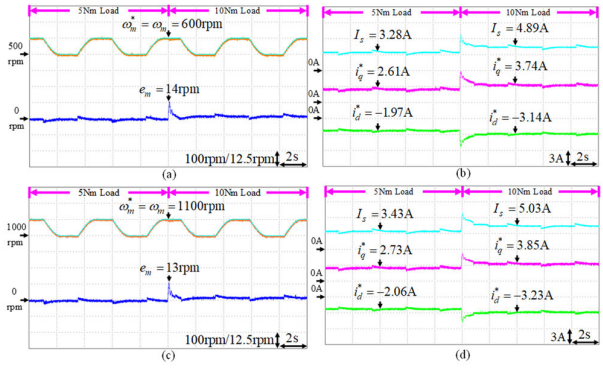

FIGURE 14. Results of ICTCRLFNN speed controller for periodical step command. (a) Rotor response and tracking error at case 1. (b) Stator and *d*-*q* axis current commands at case 1. (c) Rotor response and tracking error at case 2. (d) Stator and *d*-*q* axis current commands at case 2.

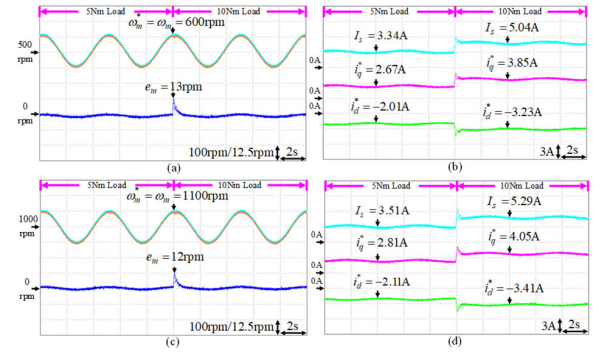

FIGURE 15. Results of ICTCRLFNN speed controller for periodical sinusoidal command. (a) Rotor response and tracking error at case 1. (b) Stator and *d*-*q* axis current commands at case 1. (c) Rotor response and tracking error at case 2. (d) Stator and *d*-*q* axis current commands at case 2.

The performance measurements of CTC and proposed ICTCRLFNN speed controllers at two operating cases with step and sinusoidal reference commands are compared in Fig. 16. The proposed ICTCRLFNN speed controller has lower values of maximum, average and standard deviation tracking errors due to its faster convergence rate and improved generalization performance. Moreover, the

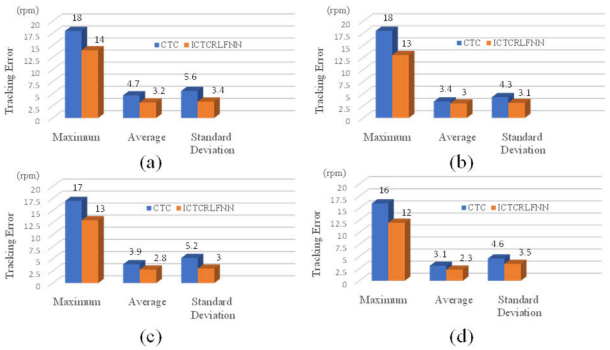

FIGURE 16. Maximum, average and standard deviation of tracking errors CTC and ICTCRLFNN. (a) Step command at case 1. (b) Sinusoidal command at case 1. (c) Step command at case 2. (d) Sinusoidal command at case 2.

execution or compute time of the "C" program in the TMS320F28075 32-bit floating point DSP with 120 MHz can be obtained by the clock tool of Texas Instruments Code Composer Studio v6 program editing interface. The total operation cycles and total execution time for the CTC are 401 and 0.00334ms; the proposed ICTCRLFNN are 7437 and 0.0619 ms, respectively. As a result, the total execution time of the proposed ICTCRLFNN is still less than 1 ms, which is the sampling interval of the speed control loop.

VI. CONCLUSION

During this study, an ICTCRLFNN is suggested to serve for a high-performance PMASynRM drive system. First, the team brings the dynamic model into play, which features an MTPA operated PMASynRM drive with ANSYS Maxwell-2D capabilities. FEA results derive an LUT, which the team uses to create the MTPA's current angle command. Subsequently, the team fashions a CTC speed tracking system. Moreover, this study suggests that RLFNN can act as a stand in for the CTC law to resolve issues with the CTC's necessary motor specifications within the PMASynRM drive. Furthermore, the Lyapunov stability method generates the RLFNN's online learning algorithms, which guarantee asymptotical stability. In the end, the experiment concludes that the suggested ICTCRLFNN has more than adequate control performance in terms of speed tracking control.

REFERENCES

[1] Z. Zhang, R. Ma, L. Wang, and J. Zhang, "Novel PMSM control for anti-lock braking considering transmission properties of the electric vehicle," *IEEE Trans. Veh. Technol.*, vol. 67, no. 11, pp. 10378–10386, Nov. 2018.

[2] Z. Qiu, Y. Chen, Y. Kang, X. Liu, and F. Gu, "Investigation into periodic signal-based dithering modulations for suppression sideband vibro-acoustics in PMSM used by electric vehicles," *IEEE Trans. Energy Convers.*, vol. 36, no. 3, pp. 1787–1796, Sep. 2021.

[3] S. Sriprang, B. Nahid-Mobarakeh, S. Pierfederici, N. Takorabet, N. Bizon, P. Kumam, P. Mungporn, and P. Thounthong, "Robust flatness control with extended Luenberger observer for PMSM drive," in *Proc. IEEE Transp. Electrific. Conf. Expo, Asia–Pacific*, Jun. 2018, pp. 1–8.

[4] S. V. Nair, P. Harikrishnan, and K. Hatua, "Six-step operation of a symmetric dual three-phase PMSM with minimal circulating currents for extended speed range in electric vehicles," *IEEE Trans. Ind. Electron.*, vol. 69, no. 8, pp. 7651–7662, Aug. 2022.

[5] S. Sriprang, B. Nahid-Mobarakeh, N. Takorabet, S. Pierfederici, P. Mungporn, P. Thounthong, N. Bizon, P. Kuman, and Z. Shah, "Maximum torque per ampere and field-weakening controls for the high-speed operation of permanent-magnet assisted synchronous reluctance motors," in *Proc. Res., Invention, Innov. Congr. (RIC)*, Dec. 2019, pp. 1–7.
[6] J.-H. Lee, Y.-J. Jang, and J.-P. Hong, "Characteristic analysis of permanent magnet-assisted synchronous reluctance motor for high power application," *J. Appl. Phys.*, vol. 97, no. 10, May 2005, Art. no. 10Q503.
[7] B. Kerdsup, N. Takorabet, and B. Nahidmobarakeh, "Design of permanent magnet-assisted synchronous reluctance motors with maximum efficiency-power factor and torque per cost," in *Proc. 13th Int. Conf. Electr. Mach. (ICEM)*, Sep. 2018, pp. 2465–2471.
[8] D. Jung, Y. Kwak, J. Lee, and C. Jin, "Study on the optimal design of PMa-SynRM loading ratio for achievement of ultrapremium efficiency," *IEEE Trans. Magn.*, vol. 53, no. 6, pp. 1–4, Jun. 2017.
[9] F.-J. Lin, Y.-C. Hung, J.-M. Chen, and C.-M. Yeh, "Sensorless IPMSM drive system using saliency back-EMF-based intelligent torque observer with MTPA control," *IEEE Trans. Ind. Informat.*, vol. 10, no. 2, pp. 1226–1241, May 2014.
[10] T. Liu, Y. Chen, M. Wu, and B. Dai, "Adaptive controller for an MTPA IPMSM drive system without using a high-frequency sinusoidal generator," *J. Eng.*, vol. 2017, no. 2, pp. 13–25, Feb. 2017.
[11] T. Sun, J. Wang, and X. Chen, "Maximum torque per ampere (MTPA) control for interior permanent magnet synchronous machine drives based on virtual signal injection," *IEEE Trans. Power Electron.*, vol. 30, no. 9, pp. 5036–5045, Sep. 2015.
[12] A. Dianov, A. Anuchin, and A. Bodrov, "Robust MTPA control for steady-state operation of low-cost IPMSM drives," *IEEE J. Emerg. Sel. Topics Ind. Electron.*, vol. 3, no. 2, pp. 242–251, Apr. 2022.
[13] F.-J. Lin, Y.-H. Liao, J.-R. Lin, and W.-T. Lin, "Interior permanent magnet synchronous motor drive system with machine learning-based maximum torque per ampere and flux-weakening control," *Energies*, vol. 14, no. 2, p. 346, Jan. 2021.
[14] Y. I. Nadjai, H. Ahmed, N. Takorabet, and P. Haghgooei, "Maximum torque per ampere control of permanent magnet assisted synchronous reluctance motor: An experimental study," *Int. J. Robot. Control Syst.*, vol. 1, no. 4, pp. 416–427, Oct. 2021.
[15] P. Niazi, H. A. Toliyat, and A. Goodarzi, "Robust maximum torque per ampere (MTPA) control of PM-assisted SynRM for traction applications," *IEEE Trans. Veh. Technol.*, vol. 56, no. 4, pp. 1538–1545, Jul. 2007.
[16] F.-J. Lin and R.-J. Wai, "A hybrid computed torque controller using fuzzy neural network for motor-quick-return servo mechanism," *IEEE/ASME Trans. Mechatronics*, vol. 6, no. 1, pp. 75–89, Mar. 2001.
[17] F.-J. Lin and R.-J. Wai, "Hybrid computed torque controlled motor-toggle servomechanism using fuzzy neural network uncertainty observer," *Neurocomputing*, vol. 48, nos. 1–4, pp. 403–422, Oct. 2002.
[18] J. C. Patra and C. Bornand, "Nonlinear dynamic system identification using Legendre neural network," in *Proc. Int. Joint Conf. Neural Netw. (IJCNN)*, Jul. 2010, pp. 1–7.
[19] D. M. Sahoo and S. Chakraverty, "Functional link neural network learning for response prediction of tall shear buildings with respect to earthquake data," *IEEE Trans. Syst., Man, Cybern., Syst.*, vol. 48, no. 1, pp. 1–10, Jan. 2018.
[20] C.-H. Lin, "Novel adaptive modified recurrent Legendre neural network control for a PMSM servo-driven electric scooter with V-belt continuously variable transmission system dynamics," *Trans. Inst. Meas. Control*, vol. 37, no. 10, pp. 1181–1196, Nov. 2015.
[21] S. Chen, F. Lin, C. Liang, and C. Liao, "Intelligent maximum power factor searching control using recurrent Chebyshev fuzzy neural network current angle controller for SynRM drive system," *IEEE Trans. Power Electron.*, vol. 36, no. 3, pp. 3496–3511, Mar. 2021.
[22] Y.-Y. Lin, J.-Y. Chang, and C.-T. Lin, "Identification and prediction of dynamic systems using an interactively recurrent self-evolving fuzzy neural network," *IEEE Trans. Neural Netw. Learn. Syst.*, vol. 24, no. 2, pp. 310–321, Feb. 2013.
[23] F.-J. Lin, S.-G. Chen, and C.-W. Hsu, "Intelligent backstepping control using recurrent feature selection fuzzy neural network for synchronous reluctance motor position servo drive system," *IEEE Trans. Fuzzy Syst.*, vol. 27, no. 3, pp. 413–427, Mar. 2019.
[24] F. Lin, I. Sun, K. Yang, and J. Chang, "Recurrent fuzzy neural cerebellar model articulation network fault-tolerant control of six-phase permanent magnet synchronous motor position servo drive," *IEEE Trans. Fuzzy Syst.*, vol. 24, no. 1, pp. 153–167, Feb. 2016.
[25] M. Sanada, S. Morimoto, and Y. Inoue, "Development of high-power PMASynRM using ferrite magnets for reducing rare-earth material use," in *Proc. Int. Power Electron. Conf.*, May 2014, pp. 3519–3524.
[26] F. Lin, Y. Liu, and W. Yu, "Power perturbation based MTPA with an online tuning speed controller for an IPMSM drive system," *IEEE Trans. Ind. Electron.*, vol. 65, no. 5, pp. 3677–3687, May 2018.

FAA-JENG LIN (Fellow, IEEE) received the B.S. and M.S. degrees in electrical engineering from National Cheng Kung University, Taiwan, in 1983 and 1985, respectively, and the Ph.D. degree in electrical engineering from National Tsing Hua University, Taiwan, in 1993. He is currently a Chair Professor with the Department of Electrical Engineering, National Central University, Taiwan. He is also the Executive Director of Taiwan Power Company. His work has been widely cited. Several of his papers have helped to establish research areas, such as fuzzy neural network control of motor drives and motion control systems, and resonant converters for piezo-ceramic motor drives. His research interests include ac motor drives, power electronics, renewable energies, smart grids, and intelligent and nonlinear control theories. He is an IET Fellow. He received the Outstanding Research Award from the National Science Council, Taiwan, in 2004, 2010, and 2013, and the Outstanding Professor of Engineering Award from the Chinese Institute of Engineers, Taiwan, in 2016. He was the Chair and a Principle Investigator of the Smart Grid Focus Center, National Energy Project Phase I and II, Taiwan, from 2011 to 2019. He was the President of the Taiwan Smart Grid Industry Association, from 2012 to 2016. He was an Associate Editor of IEEE TRANSACTIONS ON FUZZY SYSTEMS. He is also an Associate Editor of IEEE TRANSACTIONS ON POWER ELECTRONICS.

MING-SHI HUANG received the B.S. degree in electrical engineering from the National Taiwan University of Science and Technology, Taiwan, in 1987, the M.S. degree in electrical engineering from Tatung University, Taiwan, in 1991, and the Ph.D. degree in electrical engineering from National Tsing Hua University, Taiwan, in 2004. From 1987 to 2004, he was a Researcher with Mechanical Industry Research Laboratories, Industrial Technology Research Institute. He is currently a Professor with the Department of Electrical Engineering, National Taipei University of Technology, Taipei City, Taiwan. His research interests include power electronics, variable-speed drives, and electrical power train in vehicle applications.

CHUNG-YU HUNG was born in Changhua, Taiwan, in 1998. He received the B.S. degree in electrical and computer engineering from Tamkang University, Tamsui, Taiwan, in 2020. He is currently pursuing the M.S. degree in electrical engineering with National Central University, Taoyuan City, Taiwan. His research interests include DSP-based control systems, motor servo drive systems, and intelligent control theories.

YU-CHEN CHIEN was born in Taipei, Taiwan, in 1999. He received the B.S. degree in electrical and computer engineering from Tamkang University, Tamsui, Taiwan, in 2020. He is currently pursuing the M.S. degree in electrical engineering with National Central University, Taoyuan City, Taiwan. His research interests include DSP-based control systems, motor servo drive systems, and intelligent control theories.